JOURNAL OF SPACECRAFT AND ROCKETS
Vol. 40, No. 6, November–December 2003

Governing Equations for Weakly Ionized Plasma Flowfields of Aerospace Vehicles

Eswar Josyula*
U.S. Air Force Research Laboratory, Wright–Patterson Air Force Base, Ohio 45433
and
William F. Bailey†
U.S. Air Force Institute of Technology, Wright–Patterson Air Force Base, Ohio 45433

A generalized set of conservative equations for simulating the flowfield in a hypersonic weakly ionized gas flows is presented. Additional numerical and physical complexities associated with the plasma state are identified and discussed, including the influence of external and space charge fields and the nonequilibrium coupling of reactive and nonreactive collisions. A restricted set of equations is then employed to simulate and analyze the flowfield of an air plasma generated by associative ionization. With use of a seven-species air model, details of the plasma flowfields are presented and compared with available experiments. Refined estimates of dissociation products, which are the precursors to the ionization reaction, are obtained. Specific attention is given to limiting forms of the electron diffusion coefficient and the influence of vibration–dissociation coupling. Details of the chemical reactions in the flowfield influencing the elastic and inelastic collisional energy transfer are reported to highlight the more important species and reaction mechanisms.

Nomenclature

C_s = mass concentrations of species s
D_s = effective diffusion coefficient for species s, m^2/s
D_{sk} = multicomponent diffusion coefficient
$\mathcal{D}_{sk}$ = binary diffusion coefficient
$\boldsymbol{E}$ = electric field, function of space and time, V/m
E_e = translational energy of electrons per unit volume, J/m^3
e = total energy per unit mass, J/kg
$F_{\text{ela},s}$ = force per unit volume due to elastic collisions, N/m^3
$F_{\text{ele},s}$ = force per unit volume due to electric field, N/m^3
$F_{\text{inela},s}$ = force per unit volume due to inelastic collisions, N/m^3
h^0 = enthalpy of formation, J/kg
k = Boltzmann constant, 1.3807×10^{-23} J/K
L = characteristic length, m
M = Mach number
$\mathcal{M}$ = molecular weight, kg/mole
M_e = electron mass, 9.1094×10^{-31} kg
m = mass, kg
N = number density, number/m^3
$\hat{N}$ = Avogadro's number, 6.02252×10^{23}/mole
p = pressure, N/m^2
Q = energy exchange between modes, J/m^3 s
Q_{rad} = radiation heat loss term, J/m^3 s
q = charge, C
$\boldsymbol{q}^j$ = heat flux vector, W/m^2
T = translational temperature, K
T_{eff} = effective temperature at which dissociation or ionization reaction is considered, K
T_v = vibrational temperature, K
$\boldsymbol{u}^j$ = mass-averaged velocity component of mixture fluid in three dimensions, where j is 1–3
$\boldsymbol{u}_s^j$ = average or mean velocity of species s in three dimensions, where j is 1–3 m/s
$\boldsymbol{V}$ = random or peculiar velocity or diffusion velocity, m/s
$\boldsymbol{v}_s^j$ = velocity of species s in three dimensions, where j is 1–3 m/s
$\boldsymbol{X}$ = mole fraction
$\boldsymbol{x}^j$ = position vector in three dimensions, where j is 1–3 m
Z_s = ionic valency, −1 for electrons, 1 for single-ionized positive ions
Γ = electron or ion flux density, number/$m^2 \cdot s$
ε = elementary electronic charge, 1.6022×10^{-19} C
ϵ_0 = permittivity of free space, 8.8542×10^{-12} F/m
η' = thermal conductivity coefficient, W/mK
Θ_d = characteristic temperature of dissociation, K
Θ_v = characteristic temperature of vibration, K
ν = collision frequency, Hz
ν_{er}^* = effective collision frequency of electrons with diatomic molecules (heavy particles), Hz
ρ = total density, kg/m^3
ρ_n = state density in the nth vibrational level, kg/m^3
σ = collision cross section, m^2
τ = relaxation time, s
$\boldsymbol{\tau}^{ij}$ = viscous shear stress, N/m^2
ω_{pe} = electron plasma frequency, $56.4\sqrt{(N_e)}$ rad/s, where N_e is m^{-3}
$\dot{\omega}$ = source or sink of species, $kg/m^3 \cdot s$

Subscripts

D = Debye
e = electron
I = ion
n, m = vibration quantum numbers
r = diatomic molecule (heavy particle)
s = species
v = vibration
∞ = freestream conditions

Superscripts

i, j = ith and jth components in general orthogonal coordinates

Received 20 August 2002; revision received 7 May 2003; accepted for publication 22 May 2003.

*Research Aerospace Engineer, Air Vehicles Directorate, AFRL/VAAC, 2210 Eighth Street. Associate Fellow AIAA.
†Associate Professor, Department of Engineering Physics, AFIT/ENP, 2950 Hobson Way.

Introduction

THE emerging plasma applications in hypersonic flows for sustained flight in low-density environments and during atmospheric reentry are well known for their physical complexity. They offer renewed technical challenges for proper understanding of the flow physics and the physical models. The velocities and altitudes for transatmospheric missions result in thermal, chemical, and ionizational nonequilibrium conditions, more severe than those experienced in the past. The extreme environment has a major impact on the design and analysis of the vehicle aerodynamics and thermal loading. The dominant chemical kinetic processes in the plasma play an important role in the degree of electromagnetic interference surrounding the craft, the knowledge crucial to mission planners. The numerical modeling has to include the species mass, momentum, and energy equations of the neutral species and for charge particles. The influence of the charge particles on the flowfield needs to be included, as well as the elastic and inelastic collisional energy transfer mechanisms to account for the high degree of thermal, chemical, and ionizational nonequilibrium in the flowfield.

The basic governing equations in the flight regime of the aeroassisted orbital transfer vehicles are given by Lee[1] and the conservation equations for a nonequilibrium plasma by Appleton and Bray.[2] The recent interest[3,4] in the aerodynamic performance improvements of the external and internal flows in a plasma environment has prompted a number of studies to conduct experiments and extend the flowfield modeling for air vehicles to treat a weakly ionized plasma.[5–8] We begin by reviewing the basic concepts, phenomena, and nomenclature associated with the physics of ionized gases. A hierarchy of equations suitable for plasma conditions is presented, cast into a working set of equations and applied to the investigation of plasma generation in hypersonic flows.

Collision Frequency and Mean Free Path

There are two broad classes of binary collisions: elastic and inelastic. For both classes the laws of conservation of mass, momentum, and energy can be applied to the motions of the particles before and after collisions. The distinction is that in an inelastic collision, the internal energy of one or both of the particles is changed by the collision, whereas, in an elastic collision, the total translational energies are conserved. The inelastic collisions, important in plasma applications, exchange energies between the translational and the internal energies of rotational, vibrational, and electronic states. These exchanges can result in a nonequilibrium state where collisions and excited state chemistry alter flow characteristics.

For binary encounters of species A with species B, the collision frequency is given by

$$\nu_{AB} = \langle U_s \sigma N_B \rangle \tag{1}$$

where U_s is relative speed of the collision pair, σ is the cross section for a given event, and N_B is the target number density within the volume of interaction.

Between collisions the particles are considered to move in free flight, and the distance traveled between collisions is the free path. When the length of the free path varies in a statistical manner, the idea of mean free path is introduced. In general, the cross section is a function of the relative speed. The mean free path is known if the cross section and the number density are known:

$$\lambda_{\text{mfp}} = U_s/\nu = 1/\sigma N \tag{2}$$

where $\sigma \sim 10^{-20}\text{m}^2$ and $N \sim 3 \times 10^{25}$ number/m^3 at 1 atm, standard air.

Quasi Neutrality and Debye Shielding

An ideal plasma is a quasi-neutral collection of charged particles exhibiting collective behavior. For a plasma to be ideal, the physical scale of the system L must be greater than the Debye length λ_D and the observational or characteristic timescale τ must be greater than $1/\omega_{\text{pe}}$, the inverse of the plasma frequency.

In a plasma environment, macroscopic neutrality is maintained because of the mutual compensation of the space charge of the positive ions and electrons. This compensation, however, takes place in terms of spatial and temporal averages for sufficiently large volumes and sufficiently long time. When these spatial and temporal restrictions are accounted for, a plasma is said to be a quasi-neutral medium. The spatial scale length associated with quasi neutrality is the Debye length λ_D:

$$\lambda_D = \sqrt{\epsilon_0 kT \big/ N_\infty e^2} \tag{3}$$

The following are useful forms of the Eq. (3), with N and λ_D (in meters):

$$\lambda_D = 69\sqrt{T/N} \tag{4}$$

$$\lambda_D = 7430\sqrt{kT/N} \tag{5}$$

where kT is in electron volts. The corresponding temporal scale length is the inverse of the electron plasma frequency ω_{pe}:

$$\omega_{\text{pe}}^{-1} = \lambda_{D_e} \big/ \sqrt{kT_e/M_e} \tag{6}$$

This time represents the time for the average particle (electron) to traverse the Debye length.

Governing Equations

A general macroscopic balance equation for a property ϕ of species s is written as[9]

$$\frac{\partial}{\partial t}(N_s\langle\phi_s\rangle) + \frac{\partial}{\partial x^j}\left(N_s\left\langle\phi_s v_s^j\right\rangle\right) - N_s\left[\left\langle\frac{\partial\phi_s}{\partial t}\right\rangle + \left\langle u_s^j\frac{\partial\phi_s}{\partial x^j}\right\rangle + \left\langle R_s^j\frac{\partial\phi_s}{\partial v_s^j}\right\rangle\right] = \int \phi_s\left(\frac{\partial f_s}{\partial t}\right)_{\text{coll}} \mathrm{d}c_s \tag{7}$$

The first term represents the local time variation of the mean value of ϕ_s for the species s. The second term accounts for the rate of change of $\langle\phi_s\rangle$ due to the divergence of the convective flux ($N_s\langle\phi_s v_s^j\rangle$), or in other words, due to the molecules entering and leaving the volume element with velocity v_s^j. The three terms in the square brackets represent the change of $\langle\phi_s\rangle$ with 1) time, 2) position of the particles, and 3) influence of external forces, in that order. The right-hand side of the equation represents the collision term where f is the velocity distribution function for the differential volume in velocity space, $\mathrm{d}c = \mathrm{d}v_1\,\mathrm{d}v_2\,\mathrm{d}v_3$. There are a variety of formalisms for the equations describing a plasma fluid. Here we present two that are often useful. The first is a set of macroscopic equations for each species in which the equations are referred to the mean velocity of each species. The second is a velocity-weighted approach according to the mass density of the various constituents. In this approach, the macroscopic equations for each species are referred to the mass-averaged velocity and then summed over all species to obtain macroscopic equations for the entire fluid.

Species Mass Conservation

The species mass conservation equations is

$$\frac{\partial}{\partial t}\rho_s + \frac{\partial}{\partial x^j}\rho_s u^j = \frac{\partial}{\partial x^j}\left(\rho_s V_s^j\right) + \dot{\omega}_s \tag{8}$$

where V_s^j is the diffusion velocity of the species s given by

$$V_s^j = u_s^j - u^j \tag{9}$$

The mixture density is

$$\rho = \sum_s \rho_s = \sum_s N_s m_s \tag{10}$$

where ρ_s is the mass density, N_s is the number density and m_s is the particle mass of the species s. Note that $\dot{\omega}_s$ represents the production and destruction of the species s, whose sum over all of the species equals zero,

$$\sum_s \dot{\omega}_s = 0 \tag{11}$$

and the sum of the mass flux due to diffusion equals zero:

$$\sum_s \rho_s V_s^j = 0 \tag{12}$$

Contributions to $\dot{\omega}_s$ arise from such sources and sinks as dissociation, ionization, recombination, and attachment. As a simple example of the application of this set of equations in a weakly ionized flow, we consider a study of plasma generation at high Mach numbers arising from the associative-ionization reaction. The primary species of air considered in the present study are O_2, O, N_2, N, NO, NO^+, and e^-. The significant reactive collisions constituting sources and sinks in the continuity equations are[10,11]

$$\begin{gathered}
N_2 + M \rightleftharpoons 2N + M \quad (9.76\ \text{eV}) \\
O_2 + M \rightleftharpoons 2O + M \quad (5.12\ \text{eV}) \\
NO + M \rightleftharpoons N + O + M \quad (6.49\ \text{eV}) \\
N_2 + O \rightleftharpoons NO + N \quad (3.27\ \text{eV}) \\
NO + O \rightleftharpoons O_2 + N \quad (1.37\ \text{eV}) \\
N + O \rightleftharpoons NO^+ + e^- \quad (2.76\ \text{eV}) \\
NO + M \rightleftharpoons NO^+ + e^- + M \quad (9.25\ \text{eV})
\end{gathered} \tag{13}$$

where the reaction threshold for the forward (dissociation or ionization) process is given in the parentheses. The first three reactions are dissociation–recombination and the fourth and fifth are exchange reactions. The sixth reaction equation is the associative–ionization and its inverse the dissociative–recombination reaction. The net energy (2.76 eV) that must be supplied for the associative–ionization reaction of N and O is considerably less than the full ionization potential (9.25 eV) for the $NO + M \rightleftharpoons NO^+ + e^- + M$ reaction.[11] From the studies of Lin and Teare[10] and Wilson[12] for the case of air, this associative–ionization mechanism is dominant for shock speeds below 9 km/s. Above this velocity, electron-impact[12] ionization dominates. At high temperatures, additional mechanisms lead to the creation of O_2^+, O^+, and N_2^+, however, these mechanisms are not relevant in the present study addressing the lower temperature regime. Consult Refs. 13 and 14 for details on these kinetic processes.

The dissociation rates were calculated using the following functional form of the Arrhenius equation:

$$k_f(T_{\text{eff}}) = C_f T_{\text{eff}}^{\eta} \exp(\theta_d / T_{\text{eff}}) \tag{14}$$

The recombination rates were calculated from the equilibrium curve fits,

$$k_b(T_{\text{eff}}) = \frac{k_f(T_{\text{eff}})}{K_{\text{eq}}(T_{\text{eff}})} \tag{15}$$

The constants C_f, η, and θ_d and the expression for K_{eq} taken from existing experiments are tabulated in the Appendix. The reaction rates and equilibrium constants in the present study were taken from the work of Park[15] for the first five reactions and from Wray[16] for the sixth reaction. See the Appendix for details of the reaction rate coefficients. More recent work on reaction rates in air are available from the work of Park [17,18] for components of air and Bose and Candler[19] for the nitric oxide formation reaction. The species-conservation equation (8) was solved for each species, O_2, O, N_2, N, NO, NO^+, and e.

Species Momentum Conservation

The species momentum equation is given by

$$\begin{aligned}
&\frac{\partial}{\partial t}\left(\rho_s u_s^i\right) + \frac{\partial}{\partial x^j}\left(\rho_s u^i u^j\right) + \frac{\partial}{\partial x^j}\left(\rho_s u^i V_s^j + \rho_s u^j V_s^i\right) \\
&\quad + \frac{\partial p_s}{\partial x^i} - \frac{\partial \tau_s^{ij}}{\partial x^j} = F_{\text{ele},s}^i + F_{\text{ela},s}^i + F_{\text{inela},s}^i
\end{aligned} \tag{16}$$

The contributing forces F^i depend on the type of collision, elastic or inelastic, and whether the species is neutral or charged.

Because of the important role of electrons in a plasma environment, the electron momentum equation is presented with the forces written explicitly:

$$\begin{aligned}
&\frac{\partial}{\partial t}\left(\rho_e u_e^i\right) + \frac{\partial}{\partial x^j}\left(\rho_e u^i u^j\right) + \frac{\partial}{\partial x^j}\left(\rho_e u^i V_e^j + \rho_e u^j V_e^i\right) + \frac{\partial p_e}{\partial x^i} - \frac{\partial \tau_e^{ij}}{\partial x^j} \\
&\quad = -N_e \varepsilon E^i - N_e M_e \sum_r \nu_{er}^* \left(u_e^i - u_r^i\right)
\end{aligned} \tag{17}$$

The electric field E^i is associated with space charge or externally impressed on the flowfield and can be treated with different degrees of approximation.

Electric Field Models

The Poisson equation links the space charge of the plasma to the electrostatic potential ϕ. In the electrostatic approximation, the electric field is given by the negative of the gradient of ϕ. Because $\nabla \cdot \boldsymbol{E} = \zeta / \epsilon_0$, the Poisson equation is stated as

$$\nabla^2 \phi = -(\zeta / \epsilon_0) \tag{18}$$

where ζ is the total charge density given by

$$\zeta = \sum_s q_s N_s \tag{19}$$

If the individual species are analyzed separately, the total charge density may be accumulated and the electric field, accounting for the boundary conditions, can be established self-consistently through a solution of Poisson's equation. The solution, however, may be computationally expensive and introduce stringent time steps and grid requirements. Often, instead, approximate forms are introduced that do not require solution of Poisson's equation.

Equilibrium Model of Electric Field

In many circumstances of interest the pressure gradient and the electric field term in Eq. (17) dominate the momentum balance. This enables an approximate evaluation of the field:

$$E^i = -\frac{1}{N_e \varepsilon} \frac{\partial p_e}{\partial x^i} \tag{20}$$

In this approximation, the electron pressure gradient balances the forces arising from space charge or impressed fields. This approximation is convenient and often appropriate for specifying the field without resorting to a solution of Poisson's equation. For a spatially homogeneous electron temperature, this form states that the electrons achieve a Boltzmann equilibrium with the field.

Ambipolar Electric Field

When considering current flow to an insulated surface, the electric field may be evaluated using ambipolar diffusion theory. Owing to the significant disparity in the transport coefficients (diffusion and mobility) of electrons and ions, a positive space charge develops at an insulating boundary, limiting the electron flux to the surface and enhancing the flux of ions. Current continuity demands that the net current to the surface be zero. Equality of the electrons and ion fluxes defines this ambipolar condition:

$$\Gamma_e = \Gamma_I = \Gamma = D_a \nabla N \tag{21}$$

where

$$D_a \approx D_I[1 + (T_e/T_I)] \tag{22}$$

It follows that the ambipolar diffusion coefficient is much less than the electron free diffusion coefficient and greater than the ion free diffusion coefficient:

$$D_I < D_a \ll D_e \tag{23}$$

Now, $D_a = D_I$ for $T_e \ll T_I$. For isothermal plasmas, when $T_e = T_I$, Eq. (22) approximates to $D_a \approx 2D_I$. For an ambipolar assumption, the flux of electrons and ions in any region must be equal such that charge does not build up. The electric field, in this approximation, is given by

$$E^i = [(D_I - D_e)/(\mu_I + \mu_e)](\nabla N/N) \tag{24}$$

Total Momentum Conservation

Summing the individual species momentum equations yields

$$\frac{\partial}{\partial t}(\rho u^i) + \frac{\partial}{\partial x^j}(\rho u^i u^j) + \frac{\partial p}{\partial x^i} - \frac{\partial \tau^{ij}}{\partial x^j} = F^i_{\text{ele}} + F^i_{\text{ela}} \tag{25}$$

The term F^i_{ele} is the electric field force per unit volume given by

$$F^i_{\text{ele}} = \sum_s N_s e Z_s E^i \tag{26}$$

For an electrically neutral gas, F^i_{ele} is zero.

Transport Effects

The species viscosity in the present study was computed from the curve fits of Blottner et al.,[20] which are valid up to temperatures of 10,000 K in air. A more recent work on the transport properties in air based on the Chapman–Enskog theory exists (see Ref. 14). Figure 1 shows a comparison of the viscosity for the two approaches for nitrogen, oxygen, and singly ionized nitric oxide. Differences between the two approaches for the nitrogen and oxygen are neglible. For the ionized nitric oxide, the Blottner et al.[20] approach predicts a lower value than the Gupta et al.[14] approach above 2000 K. For the seven-species reaction set and temperatures considered in this study, the transport properties of Blottner et al. are used.

The species thermal conductivity was calculated from Euckens's relation (see Ref. 11). The viscosity and thermal conductivity of the mixture were computed from Wilke's semi-empirical mixing rule.[21] The thermal conductivity of the electrons was ignored because the freestream velocity considered in the present study was limited to 10 km/s and, according to Rose and Stankevics,[22] the heat conduction due to electrons does not present a serious engineering problem for flight velocities up to 16 km/s.

In the transport process of multicomponent diffusion, the flux of one component is influenced by the concentration gradient of a second component. In some cases, the first component's flux can be accelerated; in others, the diffusion can cause a temporary segregation, and in still other cases, a component can diffuse against its concentration gradient. The estimation of multicomponent diffusion coefficients in dilute gases can be accomplished using binary diffusion coefficients and the Stefan–Maxwell equations (see Ref. 23):

$$\nabla X_s = \sum_k \frac{X_s X_k}{\mathcal{D}_{sk}}(\boldsymbol{u}_k - \boldsymbol{u}_s) \tag{27}$$

where $\mathcal{D}_{sk}$ is the binary diffusion coefficient of the components s and k. The Stefan–Maxwell equations for two-temperature plasmas (see Ref. 24) were used to study[25] ion diffusion inside the shock structure for barothermal-diffusion-induced electric fields.

In the present analysis, only ordinary diffusion generated by the gradients in species concentration is considered where the diffusion mass flux follows Fick's first law of diffusion (see Ref. 26),

$$\rho_s \boldsymbol{u}_s = -\rho D_{sk} \nabla C_s \tag{28}$$

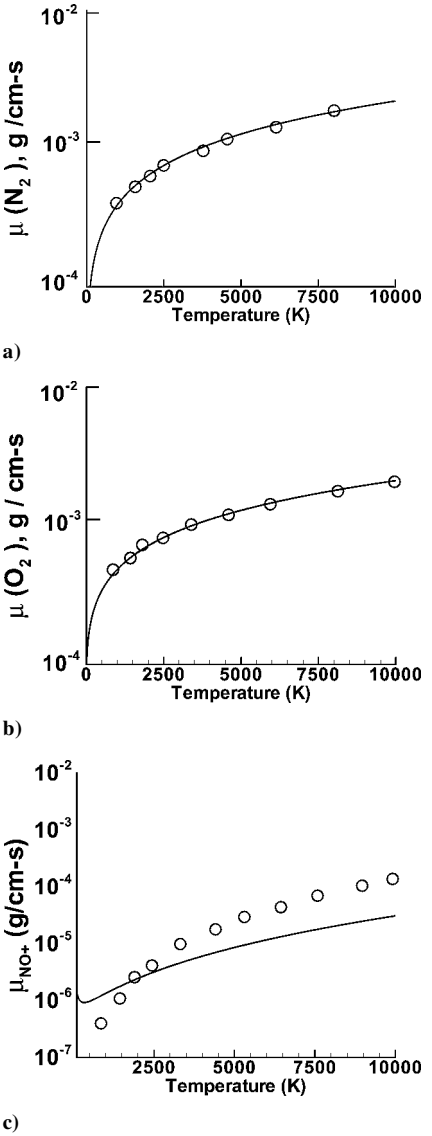

Fig. 1 Viscosity coefficient comparison by approaches in air mixture of Blottner et al.[20] and Gupta et al.[14] for a) nitrogen, b) oxygen, and c) ionized nitric oxide: ——, Blottner et al.[20] and ○, Gupta et al.[14]

where D_{sk}, the multicomponent diffusion coefficient, is calculated with a constant Lewis number 1.4. More recent work[14] on the transport properties based on the Chapman–Enskog theory was not used in the present study to be consistent with the models adopted in Ref. 27.

Species Energy Conservation

The species energy conservation equation is given by

$$\frac{\partial}{\partial t}\rho_s\left(\frac{1}{2}u^2 + u^i V^i_s + e_s\right) + \frac{\partial}{\partial x^j}\rho_s u^j\left(\frac{1}{2}u^2 + e_s\right) + \frac{\partial q^j_s}{\partial x^j}$$
$$+ \frac{\partial}{\partial x^j}\left(\frac{1}{2}\rho_s u^2 V^j_s + \rho_s u^j u^i V^i_s\right) + \frac{\partial}{\partial x^i}\left(u^i p_s\right) - \frac{\partial}{\partial x^j}\left(u^i \tau^{ij}_s\right)$$
$$= \left(\frac{\mathcal{M}_s}{\hat{N}}\right)\sum_{s,r}\dot{N}_{s_s,r}(\rho e)_{s,r} + P_{\text{ele},s} + Q_{\text{ela},s} + Q_{\text{inel},s} \tag{29}$$

Again, because of the special status of electrons in the plasma, the electron energy equation is explicitly presented.

Electron Energy Conservation

The elecron energy conservation equation is

$$\frac{\partial}{\partial t}\rho_e\left(\frac{1}{2}u^2 + u^i V_e^i + e_e\right) + \frac{\partial}{\partial x^j}\rho_e u^j\left(\frac{1}{2}u^2 + e_e\right) + \frac{\partial q_e^j}{\partial x^j} + \frac{\partial}{\partial x}\left(\frac{1}{2}\rho_e u^2 V_e^j + \rho_e u^j u^i V_e^i\right) + \frac{\partial}{\partial x^i}\left(u^i p_e\right) - \frac{\partial}{\partial x^j}\left(u^i \tau_e^{ij}\right) = \left(\frac{\mathcal{M}_e}{\hat{N}}\right)\sum_{s,r}\dot{N}_{e_{s,r}}(\rho e)_{s,r} + P_{\text{ele},s} + Q_{\text{ela},e} + Q_{\text{inel},e} \quad (30)$$

The internal energy of electrons e_e is given by

$$e_e = \frac{[3/2kT_e + \langle\epsilon_{\text{int},e}\rangle]}{\mathcal{M}_e} \quad (31)$$

The term

$$\sum_{s,r}\dot{N}_{e_{s,r}}(\rho e)_{s,r}$$

is the birthing term representing the energy gained by new-born electrons. The term, $P_{\text{ele},s}$ is the work done by the electric field on electrons, the volumetric Joule heating, given by

$$P_{\text{ele},s} = N_s \varepsilon Z_s E^i \cdot u_s^i \quad (32)$$

The translational energy transfer rate of the elastic collisions of the diatomic molecules and electrons is derived from Lee[1]:

$$Q_{\text{ela},e} = 3\overline{R}\rho_e(T - T_e)\sqrt{\frac{8\bar{R}T_e}{\pi M_e}}\sum_{s\neq e}\frac{\rho_s N}{\mathcal{M}_s^2}\sigma_{es} \quad (33)$$

where σ_{es} are the collision cross sections for electron–neutral interactions. For this work, σ_{es} equal to 10^{-20} m^2 was assumed. For the case of electron–ion interactions, the effective Coulomb cross sections are given by Lee[1]:

$$\sigma_{e,i} = \frac{8\pi}{27}\frac{\varepsilon^4}{k^2 {T_e}^2}\ell n\left[1 + \frac{9k^3 {T_e}^3}{4\pi N_e \varepsilon^6}\right] \quad (34)$$

The rate of inelastic energy exchange between electrons and molecules is given by $Q_{\text{inel},e}$:

$$Q_{\text{inel},e} = -\sum_f \dot{N}_{e,f} E_{i,f} - Q_{e-V} - Q_{\text{rad}} \quad (35)$$

It includes electron–vibration (E–V) energy transfer, radiation loss, and the electron impact ionization term

$$\sum_f \dot{N}_{e,f} E_{i,f}$$

where $\dot{N}_{e,f}$ is the rate of ionization by the fth electron-impact ionization process and $E_{i,f}$ is the first ionization energy. The energy exchanges between the inelastic collisions of the electronic and vibrational mode are discussed further in the section on vibrational conservation energy equation.

Total Energy Conservation

The total energy conservation equation is

$$\frac{\partial}{\partial t}\left[\rho\left(\frac{1}{2}u^2 + e\right)\right] + \frac{\partial}{\partial x^j}\left[\rho u^j\left(\frac{1}{2}u^2 + e\right)\right] + \frac{\partial q^j}{\partial x^j} + \frac{\partial}{\partial x^j}(u^i p) - \frac{\partial}{\partial x^j}(u^i \tau^{ij}) = \sum_s N_e \varepsilon Z_s E^i u_s^i - Q_{\text{rad}} \quad (36)$$

The calculation of temperature and pressure is as follows:

The total energy, ρe is written as the sum of the individual components of energy:

$$\rho e = \sum_{s\neq e}\rho_s C_{v_s} T + \frac{1}{2}\sum_{s\neq e}\rho_s u^i u^i + \sum \rho_s e_{v_s} + E_e + \sum_{s\neq e}\rho_s h_s^0 + \sum_{s\neq e}\rho_s e_{\text{el},s} \quad (37)$$

where the expression for the energy contained in the excited electronic states $e_{\text{el},s}$ is taken from the work of Lee.[1] The translational–rotational temperature T of the diatomic molecules is obtained from Eq. (37). The vibrational temperature of the diatomic species s is determined by inverting the expression for the energy contained in a harmonic oscillator at temperature T_{v_s}:

$$e_{v_s} = \rho(R/\mathcal{M}_s)\left[\Theta_{v_s}\Big/\left(e_s^{\Theta_v/T_{v_s}} - 1\right)\right] \quad (38)$$

The translational temperature of the electrons is established from the expression relating the electron energy E_e and the electron thermal and kinetic energy:

$$E_e = \rho_e C_{v_e} T_e + \tfrac{1}{2}\rho_e u^i u^i \quad (39)$$

The pressure is given by the sum of the partial pressures

$$p = \sum_{s\neq e}\rho_s \bar{R} T + p_e \quad (40)$$

where the electron pressure p_e is given by

$$p_e = \rho_e R_e T_e \quad (41)$$

The ratio of specific heats γ is given by $\gamma = 1 + \bar{R}/C_v$, where

$$\bar{R} = \sum C_s R_s, \qquad C_v = \sum C_s C_{v_s}$$

Vibrational Energy Conservation

The vibrational internal energy conservation can be expressed by

$$\frac{\partial}{\partial t}(\rho_s e_{v,s}) + \frac{\partial}{\partial x^j}\left(\rho_s e_{v,s} u^j\right) = \frac{\partial}{\partial x^j}\left(\eta'_{v,s}\frac{\partial T_v}{\partial x^j}\right) - \frac{\partial}{\partial x^j}\left(\rho_s e_{v,s} V_s^j\right) + Q_{T-V} + Q_{V-V} + Q_{e-V} + \dot{\omega}_s D_s \quad (42)$$

The vibrational energy conservation equation (42) is solved for each of the diatomic species O_2, N_2, NO, and NO^+ using the Landau–Teller formalism.[28] The effect of vibrational population depletion arising from nitrogen and oxygen dissociation was accounted for in the vibration–dissociation coupling process.[29] The vibrational energy $e_{v,s}$ represents the total energy in the vibrational manifold for the species s, most often assumed as a simple harmonic oscillator. The energy exchange terms given by Q represent the exchange of energy between the translational and the internal energy modes of the vibrational and electronic modes.

An alternate and more detailed approach for accounting the vibrational energy is to solve the vibrational master equations. The kinetic coefficients of the particle exchanges among the quantum states give the population distributions,[30]

$$\dot{\omega}_n = \frac{1}{\mathcal{M}}\left\{\sum_{n'}[k_{VT}(n' \to n)\rho_{n'}\rho - k_{VT}(n \to n')\rho_n\rho] + \sum_{n,m,n',m'} \times [k_{VV}(n', m' \to n, m)\rho_{n'}\rho_{m'} - k_{VV}(n, m \to n', m')\rho_n\rho_m]\right\} \quad (43)$$

Energy Exchanges Between Vibrational and Other Energy Manifolds

The translational–vibrational coupling is modeled according to the Landau–Teller[28] form, which assumes single quantum exchange,

$$\dot{e}_v = \rho_s \left(e^*_{v_s} - e_{v_s}\right) \big/ \tau_s \tag{44}$$

The relaxation time is computed as

$$\tau_r = \frac{\sum_r X_r}{\sum_r X_r / \tau_{rk}} \tag{45}$$

The Landau–Teller interspecies relaxation times τ_{rk} are computed using the expression developed by Millikan and White.[31] The vibration–dissociation coupling for neutral species considering vibration–translation exchanges for nitrogen follows the approach outlined in Ref. 29. This earlier work[29] presented the effect of dissociation on the vibrational population depletion for a ladder model. The vibration–vibration exchanges and their effect on the population depletion model previously reported[32] are neglected in the present study.

The temperatures governing the reaction rates of the ionized nitric oxide and the electrons are postulated by Park in Refs. 15, 33, and 34. When the impacting particle is an electron, the associative-ionization rate is an average of the vibrational and electron temperatures, $T_{\text{eff}} = \sqrt{(T_v T_e)}$ and the dissociative-recombination rate is an average of the translational temperature of diatomic molecules and electron temperatures. For the exchange reactions, the forward and backward rates depend on the translational temperature of diatomic molecules, alone.

The associative-ionization reaction rate depends on the translational temperature, but the dissociative-recombination rate depends on the vibrational temperature of NO+ and the translational temperature of electrons.[27]

The E–V energy exchange for the nitrogen molecules is assumed to be of the Landau–Teller form (see Ref. 11)

$$Q_{\text{E-V}} = N_e[\epsilon_{vs}(T_e) - \epsilon_{vs}]/\tau_{es} \tag{46}$$

where the rate of (E–V) energy transfer τ_{es} is derived by Lee.[35]

Simplified Set of Conservation Equations

The simplified set of conservation equations was simplified and adapted to the analysis of a weakly ionized flowfield. The equilibrium electric field model [Eq. (20)] was used in the total momentum and energy equations. The simplified form follows.

Species mass conservation equation:

$$\frac{\partial}{\partial t}\rho_s + \frac{\partial}{\partial x^j}\rho_s u^j = \frac{\partial}{\partial x^j}\left(\rho_s V_s^j\right) + \dot{\omega}_s \tag{47}$$

Total momentum conservation equation:

$$\frac{\partial}{\partial t}(\rho u^i) + \frac{\partial}{\partial x^j}(\rho u^i u^j) + \frac{\partial p}{\partial x^i} - \frac{\partial \tau^{ij}}{\partial x^j} = \sum_s N_s e_s Z_s E^i \tag{48}$$

Electron energy conservation equation:

$$\frac{\partial}{\partial t}(\rho_e e_e) + \frac{\partial}{\partial x^j}\rho_e u^j \left(\frac{1}{2}u^2 + e_e\right) + \frac{\partial q_e^j}{\partial x^j} + \frac{\partial}{\partial x^i}\left(u^i p_e\right)$$
$$= \sum_{s,r} \dot{N}_{e_{s,r}} E_{s,r} + P_{\text{ele},s} + Q_{T-e} - \sum Q_{e-v} + e_{e_s}\dot{\omega}_s \tag{49}$$

Total energy conservation equation:

$$\frac{\partial}{\partial t}\left[\rho\left(\frac{1}{2}u^2 + e\right)\right] + \frac{\partial}{\partial x^j}\left[\rho u^j\left(\frac{1}{2}u^2 + e\right)\right] + \frac{\partial q^j}{\partial x^j} + \frac{\partial}{\partial x^j}(u^i p)$$
$$- \frac{\partial}{\partial x^j}(u^i \tau^{ij}) = \sum \varepsilon N_s Z_s E^i u_s^i \tag{50}$$

Vibrational energy conservation equation

$$\frac{\partial}{\partial t}(\rho_s e_{v,s}) + \frac{\partial}{\partial x^j}\left(\rho_s e_{v,s} u^j\right) = \frac{\partial}{\partial x^j}\left(\eta'_{v,s}\frac{\partial T_v}{\partial x^j}\right) - \frac{\partial}{\partial x^j}\left(\rho_s e_{v,s} V_s^j\right)$$
$$+ Q_{T-V} + Q_{e-V} + \dot{\omega}_s D_s \tag{51}$$

Numerical Procedure

The flowfield equations (47–51) were numerically solved using the Roe approximate Riemann solver. The numerical scheme is implemented in finite volume formulation by computing the cell interface flux as a summation of wave speeds as described by Walters et al.[36] The second-order spatial accuracy is obtained by employing the MUSCL approach in conjunction with the minmod limiter to reduce the solution to first-order accuracy in the vicinity of strong shock waves, as described in the work of Josyula and Shang.[37] The entropy correction for the Roe scheme is implemented as discussed in Ref. 37. The viscous terms are evaluated using central differencing. An explicit predictor–corrector method is used to advance the solution in time. This approach was discussed for the flux-splitting option by MacCormack in Ref. 38. The presence of free electrons give rise to an additional characteristic wave speed[39] for the translational temperature associated with the electrons. However, the wave speed obtained in Ref. 39 is not invariant to a Gallilean transformation.[40] A corrected form of the wave speed associated with the free electrons was subsequently presented in the Ref. 40, with the equations cast in non-conservation form which are unsuitable for the present upwind scheme. Hence, a fourth eigenvalue associated with the free electrons was not used in the present study. An alternative approach of determining eigenvalues and eigenvectors was investigated by Taylor et al.,[41] where a separate rotational energy equation was solved, thereby, decoupling the diatomic-molecule (heavy particle) equations from the electron energy equation. However, the present approach treats the translational and rotation energy modes to be in thermodynamic equilibrium.

The flow conditions of the numerical simulation based on existing experiments are given for a Mach 16.3 and 23.9 cases in Table 1. The geometry details and minimum grid spacing are in Table 2. Performance of a grid study on the Mach 23.9 case is presented for the following grid sizes (axial x normal): 1) 30×50, 2) 50×60, and 3) 70×90. The effect of the grid sizes on the translational temperature distribution along the stagnation streamline is shown in Fig. 2. The coarse grid of 30×50 nodes has a lower translational temperature than the medium grid of 50×60 nodes and fine grid of 70×90 grid. The magnitude of the Richardson extrapolation error estimator (see Ref. 42) for the peak translational temperature using the coarse and medium grids gives 2.65% and using the medium and fine grids gives 1.15%. The medium grid with 50×60 nodes in the axial and normal direction, respectively, was considered adequate and used for the Mach 23.9 case. A similar grid study conducted for the Mach 16.3 case resulted in the use of 40×50 nodes in the axial and normal directions.

Table 1 Details of flow conditions

Mach number	Re_∞	T_∞, K	T_{wall}, K	p_∞, Pa	Kn_∞	R_n, m	Altitude, km
16.3	3,750	240	1,000	12.4	4.3×10^{-3}	0.0762	64.6
23.9	19,500	254	1,500	19.7	1.2×10^{-3}	0.1524	61

Table 2 Details of grids considered

Mach number	$\Delta n^{\text{a}}/R_n$	$\theta^{\text{b}}_{\min}$	R_n, m	Length, m	Type body	Cone half-angle, deg
16.3	4.8×10^{-4}	0.45	0.0762	0.135	Sphere–cone	10
23.9	4.8×10^{-4}	1.83	0.1524	1.295	Sphere–cone	9

[a]Minimum (full-cell) grid spacing. [b]Minimum angular spacing (degree).

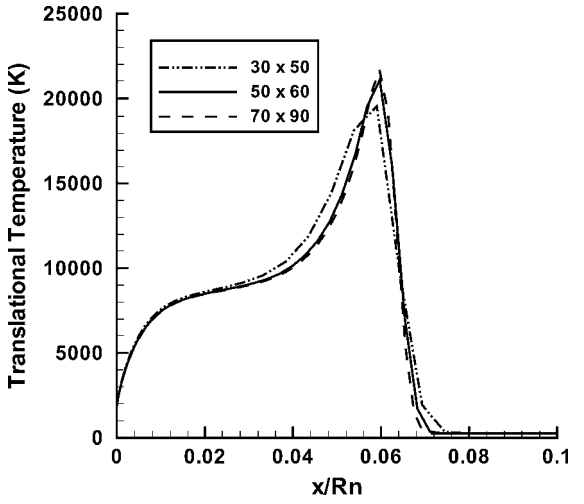

Fig. 2 Grid study: temperature distribution along stagnation streamline of RAM-C II, $M_\infty = 23.9$, $Rn = 0.1524$ m, and altitude = 61 km.

Shock Tunnel Experiments of Kaegi and McMenamin[43]

In this experiment, a reflected nozzle shock tunnel was used to produce hypersonic airflows about a 0.0762-m-nose radius hemisphere–cone. Electron–ion concentrations were determined from current measured with langmuir probes. The test conditions had velocities of 4.5 km/s (Mach 16.3) and 6 km/s (Mach 20.8) with densities corresponding to 64.6- and 58.7-km altitudes, respectively. Electron densities were measured along the stagnation streamline of the sphere–cone for the Mach 16.3 and 20.8 cases at 64.6- and 58.7-km altitudes, respectively. The conditions of the Mach 16.3 case at 64.6 km altitude (Table 1) were simulated in the present study.

Flight-Test Data from the RAM-C II

In the 1960s, the flight-test data was obtained using experimental probes at satellite speeds, called Radio Attenuation Measurement (RAM)-C tests, which measured electron number densities in the flowfield.[44–46] Conditions of the second test, RAM-C II, were simulated by several researchers, for example, Refs. 27 and 47. The wall was assumed fully noncatalytic to be consistent with the work of Ref. 27 and the temperature was fixed[48] at 1500 K, an estimate of an unknown wall temperature. The conditions of Mach 23.9 at altitude of 61 km were simulated in the present study. The body geometry was a sphere–cone of 0.1524 m radius, length of 1.295 m, and a cone half-angle of 9 deg (Table 1).

The flowfield equations (47–51) were solved to simulate the conditions described in the experiments. The seven-species reaction set [Eq. (13)] was implemented via the species mass conservation equations. The reaction set includes the associative-ionization and dissociative-recombination reaction equation for generating the weakly ionized plasma. The electric field was computed using the equilibrium model [Eq. (20)]. However, the ambipolar diffusion coefficient for the charged particles was computed using Eq. (22) and the limiting forms discussed in that section. The limiting forms for isothermal and nonisothermal plasmas provide the bounds of the diffusion coefficient for the ambipolar condition. The vibrational energy equation was solved using the Landau–Teller[28] approximation [Eq. (44)] for computing the single quantum energy exchange in the vibrational–translational mode. The vibration–dissociation coupling for the neutral species of oxygen and nitrogen was implemented using the model based on the master equations (43) accounting for the depletion of vibrational population due to dissociation. (See Ref. 29 for more details about the vibration–dissociation coupling model.) The coupling model for the elastic collisions involving the remaining species of nitric oxide and the charged particles was implemented using the Park model,[23] discussed earlier.

Boundary Conditions

The upstream and farfield boundary conditions were prescribed as the undisturbed freestream values. At the downstream boundary, the no-change condition was imposed for the predominantly supersonic flowfield. On the body surface, the no-slip condition for velocity components, an isothermal wall, and the approximation of zero normal pressure gradient were enforced. The species concentrations were set to the noncatalytic wall boundary condition for all cases. The gradient of the electron translational temperature was set to zero as per Park.[13] For the axisymmetric configuration, the boundary conditions were set at the axis of symmetry inasmuch as the product of the flux and area is zero because in a finite volume formulation the control volume surface at the axis of symmetry merges to a point.

Results and Discussion

Relaxation Zone and Flowfields Considered

The relaxation zone in a hypersonic air plasma flowfield is shown in Fig. 3. For a high-Mach-number airflow, the dissociation products of nitrogen and oxygen downstream of the shock recombine to form nitric oxide molecules which ionize at the high temperatures. Free electrons are produced in the flowfield in this associative-ionization reaction of nitric oxide. Owing to the disparity of the electron and ion diffusion coefficient, there is an excess of free electrons ahead of the shock wave, leaving positive charges behind it. This space charge generates an electric field, which results in a net force on the flowfield. At the surface edge of the weakly ionized gas, the plasma is positively charged with respect to the wall, the nonneutral region between the plasma and wall forming a plasma sheath in the flowfield. The gas can typically be assumed to behave quasi neutrally far away from the body and in the region between the shock and the body. The internal energy modes of vibration and ionization mechanisms relax in the shock layer and approach equilibrium near the surface.

Figures 4 and 5 show the sources and sinks of the chemical reactions [Eq. (13)] and the net source terms on the right-hand side of the species mass conservation equations (8) and (47). The plotted rates are the product of the rate coefficient and density of the species (mole per cubic meter per second). The values presented are along the stagnation streamline for the RAM-C II flowfield. The translational temperature is shown for reference. Figure 4 shows the forward and backward reaction rates of the forward (dissociation) and backward (recombination) reactions in air: the first three reactions in Eq. (13). The nitrogen dissociation reaction is presented in Fig. 4a, oxygen in Fig. 4b, and nitric oxide in Fig. 4c. The higher forward rates for these reactions (Figs. 4a and 4b) are responsible for the dissociation of nitrogen and oxygen. The nitric oxide dissociation reaction (Fig. 4c) results in atomic nitrogen and oxygen. The recombination reactions for the nitrogen and oxygen increase sharply in the postshock region and then increase gradually to reach a maximum near the body. The exchange reactions of nitric oxide

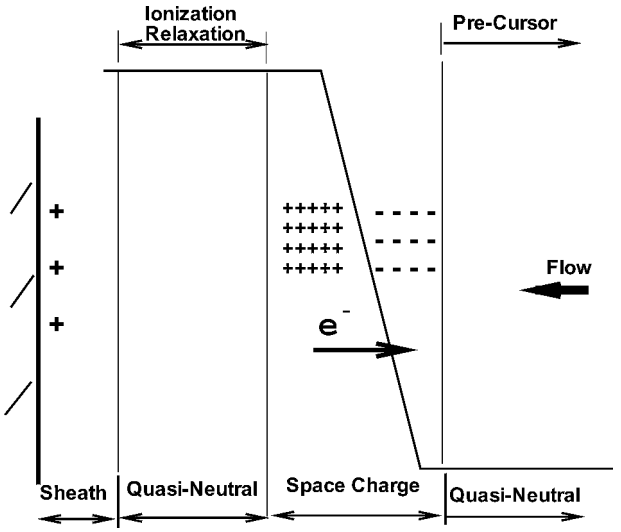

Fig. 3 Relaxation zone in shock layer.

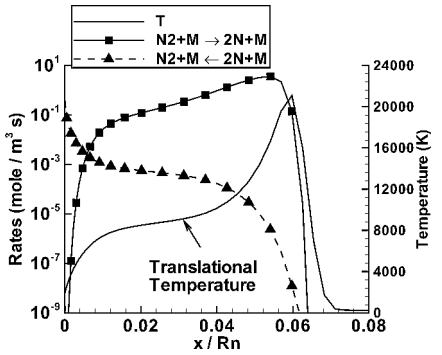

a) $N_2 + M \Leftrightarrow 2N + M$

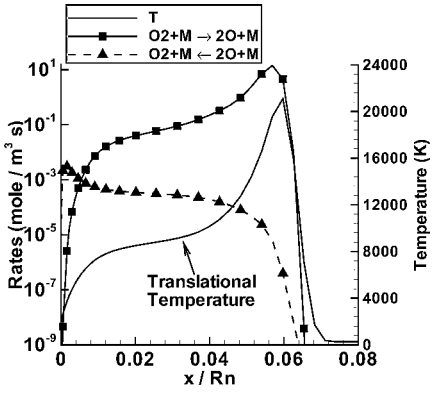

b) $O_2 + M \Leftrightarrow 2O + M$

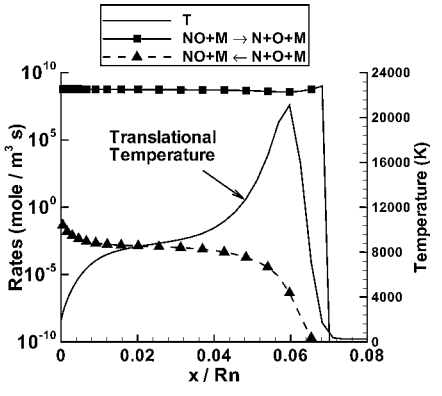

c) $NO + M \Leftrightarrow N + O + M$

Fig. 4 Forward and backward rates distribution along stagnation streamline of RAM-C II, $M_\infty = 23.9$, $Rn = 0.1524$ m, and altitude = 61 km.

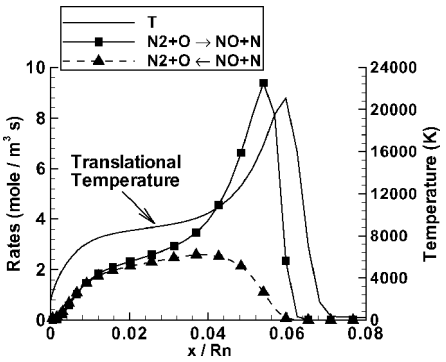

a) $N_2 + O \Leftrightarrow NO + N$

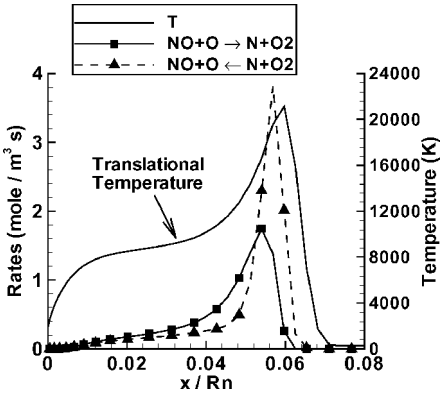

b) $NO + O \Leftrightarrow N + O_2$

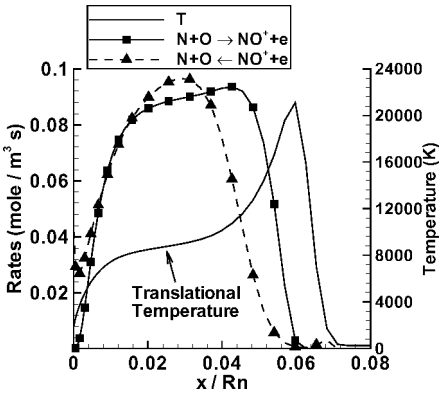

c) $N + O \Leftrightarrow NO^+ + e^-$

Fig. 5 Forward and backward rates distribution along stagnation streamline of RAM-C II, $M_\infty = 23.9$, $Rn = 0.1524$ m, and altitude = 61 km.

are shown in Figs. 5a and 5b and the associative-ionization reaction with its inverse dissociative-recombination reaction in Fig. 5c. The higher forward rates of the exchange reactions of nitric oxide are responsible for the formation of the nitric oxide (Figs. 5a and 5b). The associative-ionization reaction (Fig. 5c) is responsible for the formation of ionized nitric oxide. However, for the backward exchange reactions (Figs. 5a and 5b) and the dissociative-recombination reaction in Fig. 5c, the reaction rates peak slightly upstream of the shock and gradually increase behind the shock, reach a maximum, and fall as they approach the body. The Arrhenius form of the forward rate and significant activation energy leads to an exponential temperature sensitivity and peaks downstream of the shock. The backward rate is similarly controlled by the reactant concentration.

Figure 6 shows the resulting mass concentrations of the species, along the stagnation streamline for the RAM-C II flowfield. Oxygen is fully dissociated behind the shock wave, and nitrogen molecules are dissociated with a mass fraction of 0.34 near the surface. Nitric oxide formation peaks at a normalized location (x/Rn) of 0.05 in the postshock region. This maximum corresponds with the maxima in the reactions contributing to the nitric oxide formation: $N_2 + O \rightarrow 2NO + N$ (Fig. 5a) and $NO + O \leftarrow N + O_2$ (Fig. 5b).

The translational and vibrational temperatures for the two cases computed in the present study are presented in Figs. 7 and 8. The primary difference in the flowfields between the two cases are that the higher-Mach-number case has a smaller shock-standoff distance and a greater relaxation of the internal energy modes in the shock layer.

The highest temperature is about 22,000 K for the RAM-C II case (Fig. 7) and 13,000 K for the simulation of the experiment (Fig. 8). For the RAM-C II case, we see from Fig. 6 that dissociation results in the maximum concentration of atomic nitrogen of 40% near the surface, oxygen is fully dissociated, nitric oxide concentration peaks in the postshock region at 6%, and the maximum concentration of NO^+ is less than 0.2% in the shock layer. Nitric oxide is formed primarily by the exchange reaction, $N_2 + O \rightleftharpoons NO + N$, in the vicinity of the shock front. The electron temperature is small in the postshock region, increases to a maximum inside the shock layer,

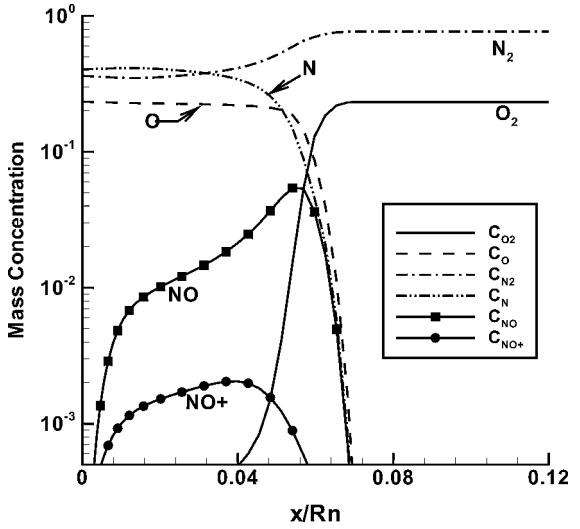

Fig. 6 Mass concentration distribution along stagnation streamline of RAM-C II, $M_\infty = 23.9$, $Rn = 0.1524$ m, and altitude = 61 km.

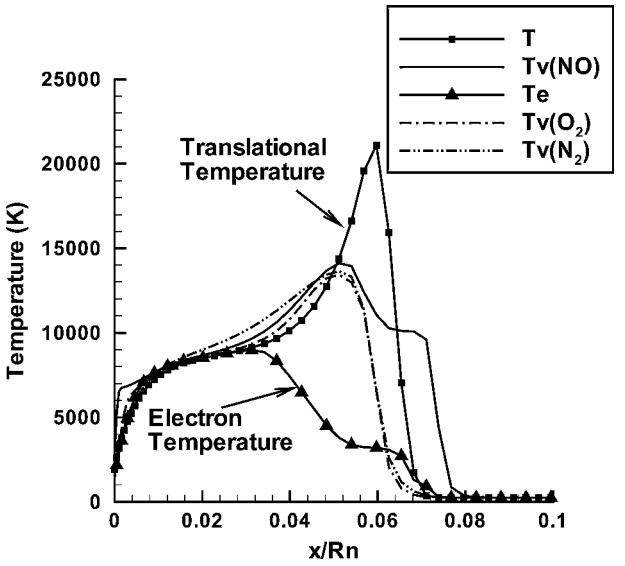

Fig. 7 Temperature distribution along stagnation streamline of RAM-C II, $M_\infty = 23.9$, $Rn = 0.1524$ m, and altitude = 61 km.

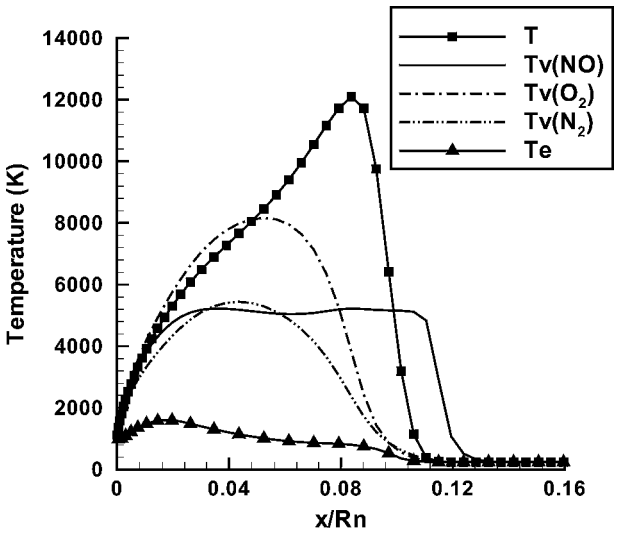

Fig. 8 Temperature distribution along stagnation streamline of experiment, $M_\infty = 16.3$, $Rn = 0.0762$ m, and altitude = 64.6 km.

and then decreases to achieve equilibrium at the surface. The electron temperature achieves equilibrium with the translational mode at $x/Rn = 0.03$ for the RAM-C II case (Fig. 7).

The two cases (Figs. 7 and 8), however, show the same peculiar feature upstream of shock: The nitric oxide vibrational temperature rises upstream of the translational temperature rise. This feature is further discussed subsequently. Note that, despite small amounts of NO and NO^+ upstream of the shock (shown later), the efficient transfer of vibrational–translational energy raises the vibrational temperatures significantly.

Figure 9 shows the Debye length along the stagnation streamline of the RAM-C II. The mean free path in the air medium shown on the same plot is computed, assuming a constant value for the collision cross section of 10^{-20} m^2. The shock wave is about 2 mm thick and is about two orders of magnitude smaller than the nose radius.

Figure 10 shows the Debye length along the stagnation streamline of the simulation of an experiment.[43] In both cases, we find $L > \lambda_D$ satisfying the ideal plasma condition. The characteristic length L is the radius of the body.

Vibrational Population Depletion Effects and Diffusion Studies

The effect of the dissociation-induced vibrational population depletion on the temperature and electron density distributions is shown in Figs. 11–13. The role of the diffusion on the spatial redistribution of the charged particles is shown in Figs. 14–18.

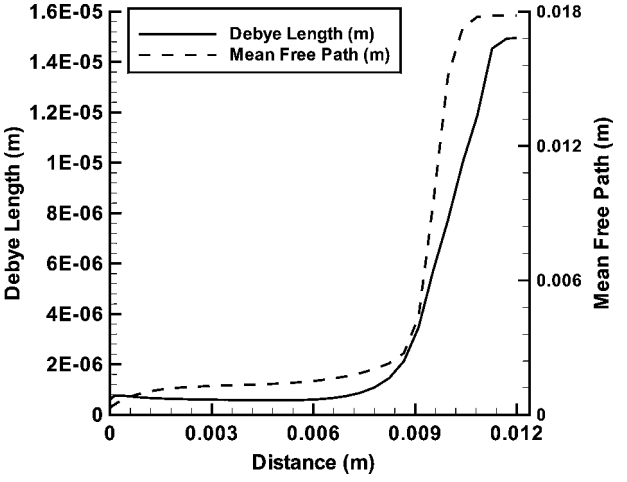

Fig. 9 Debye length and mean free path along the stagnation streamline of RAM-C II, $M_\infty = 23.9$, $Rn = 0.1524$ m, and altitude = 61 km.

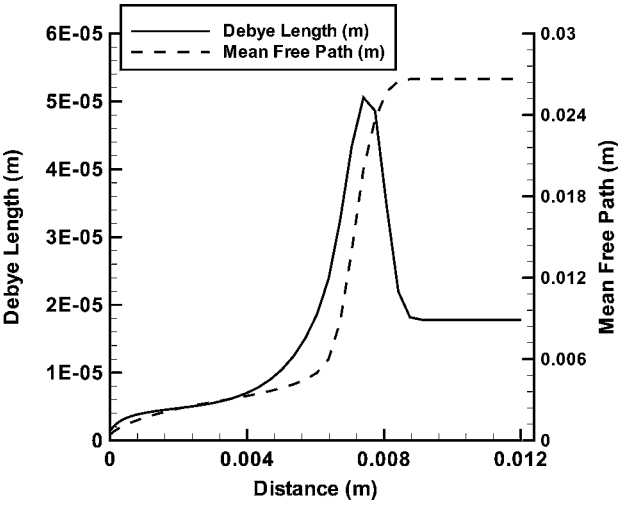

Fig. 10 Debye length and mean free path along the stagnation streamline of experiment of Kaegi and McMenamin,[43] $M_\infty = 16.3$, $Rn = 0.0762$ m, and altitude = 64.6 km.

The effect of population depletion of oxygen is expected to be negligible at these high temperatures,[49] and so only nitrogen depletion is included in this study. The peak translational temperature remains the same (Figs. 11 and 12); however, the shock standoff distance increases slightly due to depletion effects. The forward dissociation rate of the diatomic nitrogen is reduced by one to two orders of magnitude at temperatures below 10,000 K as a result of population depletion in the vibrational levels. The effect on the vibrational temperatures of nitrogen and nitric oxide is minor (Fig. 11).

The flight-test data points shown in the Figs. 13–15 were taken from Ref. 46. The microwave reflectometer measurements are shown by square symbols, and the electrostatic probe measurement at $x/Rn \sim 8$ is shown by a triangle with error bar. The reflectometer data point represents the averaged peak electron densities, and the probe data point represents the time-average electron densities for the innermost and outermost probes. The error bar on the probe data point represents the peak-to-peak density fluctuation due to body motions. The predicted electron density distribution along the noncatalytical surface compared with flight-test data shows a negligible effect due to depletion (Fig. 13). The high temperatures in the

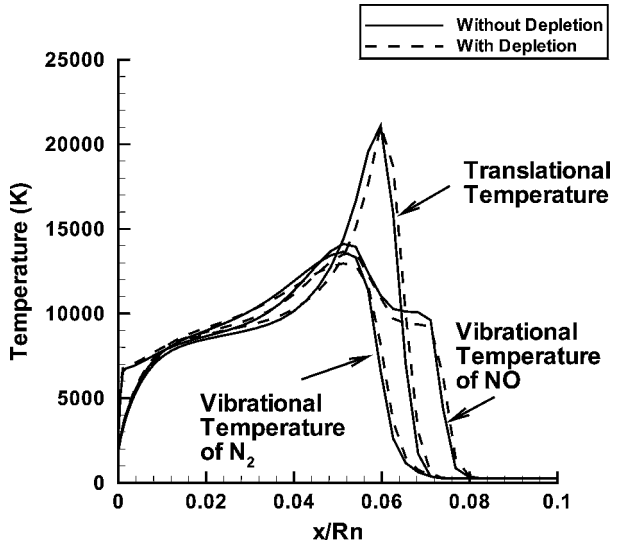

Fig. 11 Depletion effects: temperature distribution along stagnation streamline of RAM-C II, $M_\infty = 23.9$, $Rn = 0.1524$ m, and altitude = 61 km.

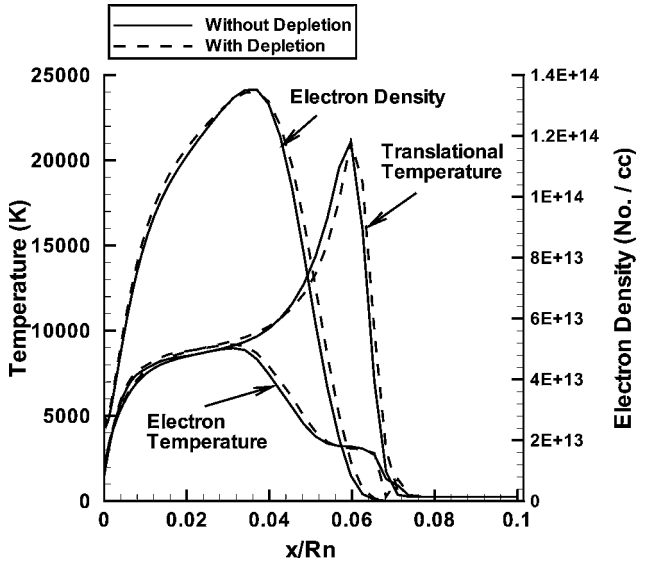

Fig. 12 Depletion effects: temperature distribution along stagnation streamline of RAM-C II, $M_\infty = 23.9$, $Rn = 0.1524$ m, and altitude = 61 km.

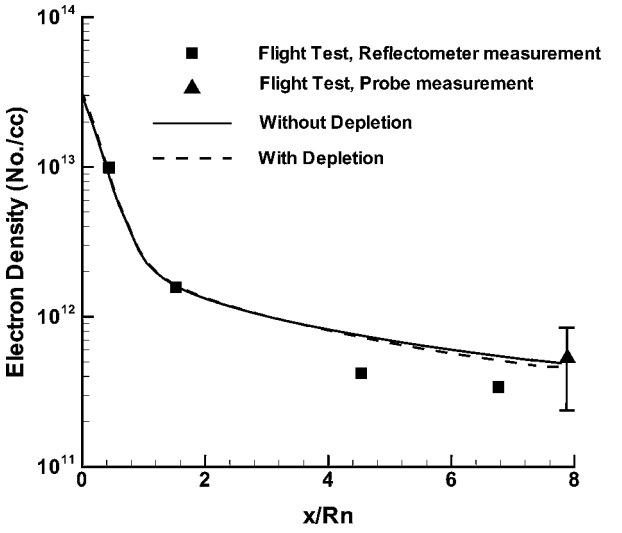

Fig. 13 Depletion effects: comparison of electron density distribution along surface with flight-test data of RAM-C II, $M_\infty = 23.9$, $Rn = 0.1524$ m, and altitude = 61 km.

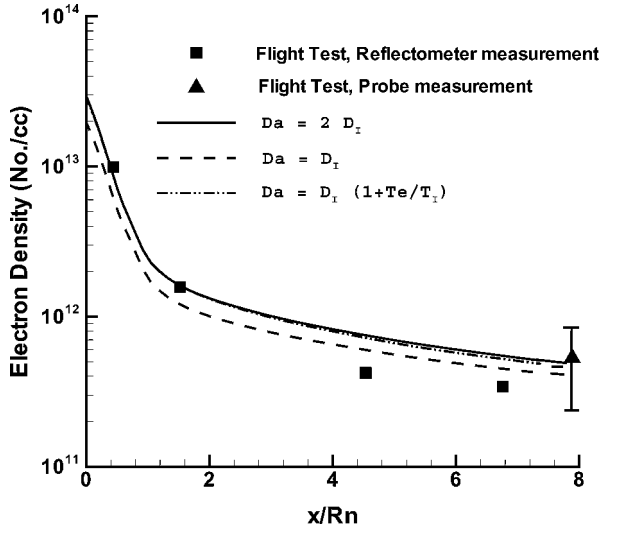

Fig. 14 Validity of approximations of ambipolar diffusion coefficient: comparison of electron density distribution along surface with flight-test data of RAM-C II, $M_\infty = 23.9$, $Rn = 0.1524$ m, and altitude = 61 km.

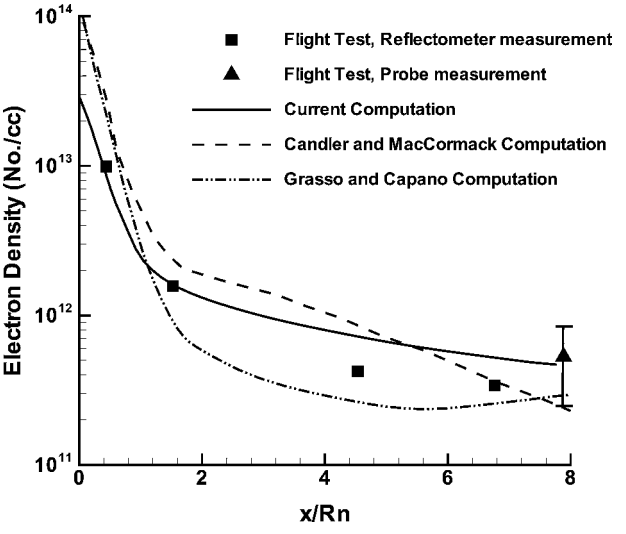

Fig. 15 Comparison of computational predictions of electron density distribution along surface with flight-test data of RAM-C II, $M_\infty = 23.9$, $Rn = 0.1524$ m, and altitude = 61 km.

postshock region and the near-equilibrium values near the surface are not favorable for dissociation-induced vibrational population depletion.[29]

The role of diffusion on the spatial redistribution of the charged particles in Figs. 14–18 is now discussed. The ambipolar diffusion is modeled in the present study per Eq. (22), $D_a \approx D_I[1 + (T_e/T_I)]$. For the two limiting cases of $Te \sim T_I$ and $Te \ll T_I$, the ambipolar diffusion coefficients of $D_a = 2D_I$ and $D_a = D_I$ were used in predicting electron density in the shock layer and near the surface.

With reference to Fig. 14, the electron density prediction near the surface with the $D_a = 2D_I$ approximation is very close to $D_I[1 + (T_e/T_I)]$, suggesting the validity of this approximation for the ambipolar diffusion coefficient for this case because $T_e \sim T_I$. This approximation is confirmed by the translational and electron temperature distributions of Fig. 7. Comparison of the present calculations for the limiting case of $D_a = 2D_I$ with the calculations of Candler and MacCormack[27] and Grasso and Capano[47] is shown in Fig. 15. Although there are modeling differences between the

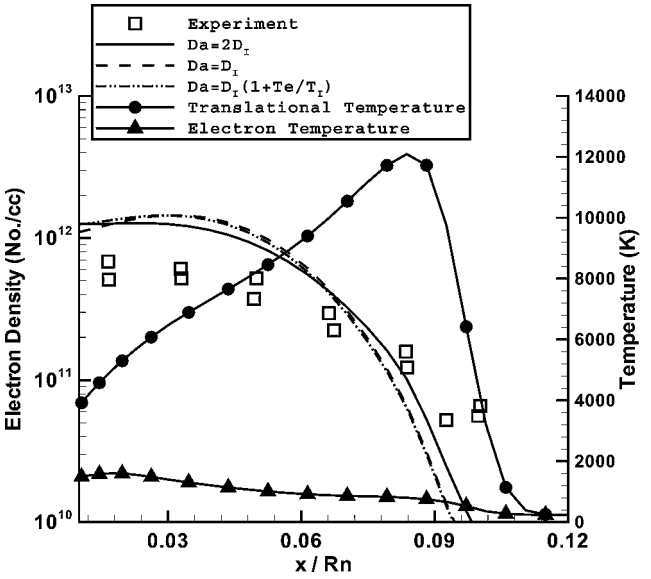

Fig. 16 Validity of approximations of ambipolar diffusion coefficient: comparison of electron density distribution along stagnation streamline with experiment, $M_\infty = 16.3$, $Rn = 0.0762$ m, and altitude = 64.6 km.

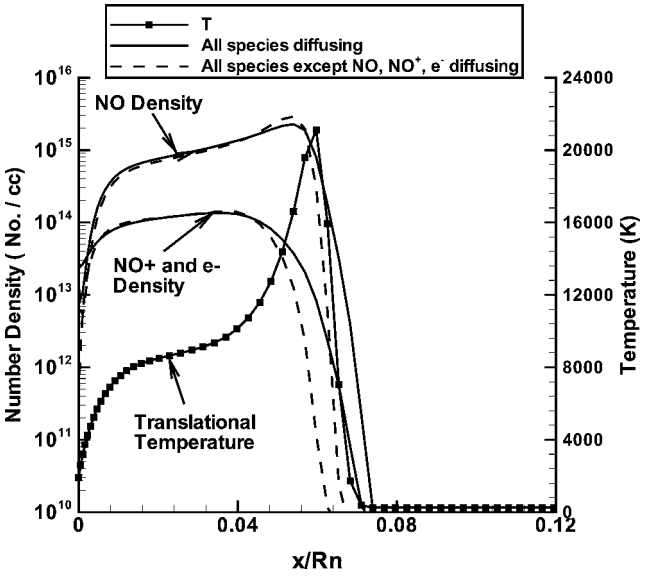

Fig. 17 Diffusion upstream of shock: density of NO, NO^+, and e^- along stagnation streamline of RAM-C II, $M_\infty = 23.9$, $Rn = 0.1524$ m, and altitude = 61 km.

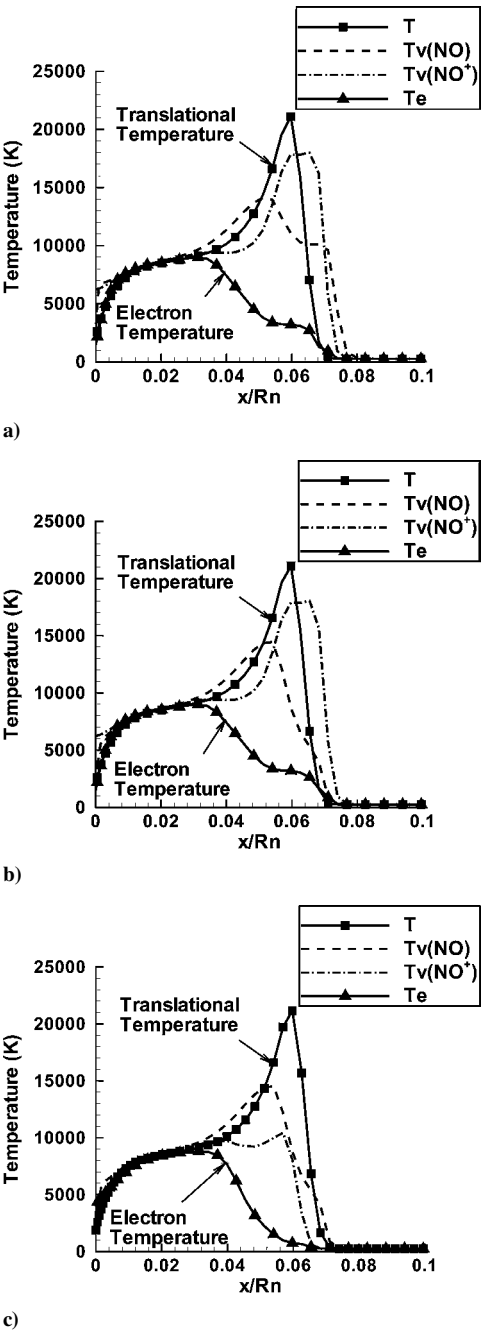

Fig. 18 Diffusion upstream of shock: temperatures along stagnation streamline of RAM-C II, $M_\infty = 23.9$, $Rn = 0.1524$ m, and altitude = 61 km: a) all species diffusing, b) all species except NO diffusing, and c) all species except NO, NO^+, and e^- diffusing.

three computations shown, all computational results fall within the experimental uncertainty of the probe data point at $x/Rn \sim 8$. More accurate experimental measurements are required to delineate and validate the models used for vibration, dissociation and ionization in the computations.

For the experimental flow conditions along the stagnation streamline of Kaegi and McMenamin[43] (Fig. 16), the electron density prediction with the limiting case approximation of $D_a = D_I$ is close to the prediction with $D_I[1 + (T_e/T_I)]$. The validity of this approximation is confirmed by $Te \ll T_I$ (Fig. 8). The electron density is lowest near the shock and reaches a maximum near the surface. The high density near the body surface is achieved through rapid diffusion of electrons. The computation overpredicts the data near the surface and underpredicts in the postshock region.

The effect of the diffusion of the nitric oxide on the density of NO, NO^+, and e^- is shown in Fig. 17. Figure 17 shows that suppressing

the diffusion of NO, NO^+, and e^- does indeed shift the rise in density of nitric oxide (consequently NO^+ and e^-) to the back of the shock wave (marked by the rise in the translational temperature). The nitric oxide ions and electrons have densities that are essentially equal. Note that the nitric oxide concentration in the freestream (ahead of the shock wave) is specified in the computations to be negligibly small. Therefore, any formation of nitric oxide ahead of the shock wave is solely due to the direction of the diffusion velocity opposite to the flow direction, thus, bringing the molecules upstream of the shock.

The effect of further numerical experiments to determine the individual role of the diffusion velocity of the nitric oxide and charged particles on the flowfield is discussed next. Figure 18a shows the translational and vibrational temperatures along the stagnation streamline of the RAM-C II for all species diffusing, Fig. 18b for all of the species except NO diffusing, and Fig. 18c for all of the species except NO, NO^+, and e^- diffusing. As stated before, there is a significant rise in the vibrational temperatures of NO and NO^+ upstream of the translational temperature rise (Fig. 18a). When the diffusion of NO molecules is suppressed (Fig. 18b), the vibrational temperature of NO shifts downstream, but the vibrational temperature of NO^+ is affected very little.

When the diffusion of NO, NO^+, and e^- is suppressed (Fig. 18c), both profiles of the vibrational temperatures of NO^+ and NO shift downstream. The vibrational temperature of NO^+ drops below that of NO. The electron temperature is lowered in Fig. 18c, primarily in the postshock region but equilibrates with the translational temperature, as in Figs. 18a and 18b. The diffusion of these particular species has small effect on the magnitude of the electron temperature and the density of the charged particles (Fig. 17) downstream of the shock wave and near the surface.

Conclusions

The study was undertaken to probe the physical complexities involved in the modeling of the emerging plasma technologies applied to hypersonic vehicles. A generalized set of governing equations for the numerical modeling of the hypersonic weakly ionized plasma flowfields about aerospace vehicles are written. A simplified set of equations was exercised to investigate a simulated ionized flowfield in air. The objectives of the simulation were to 1) assess the magnitude and spatial distribution of the atomic densities arising from dissociation, 2) evaluate the importance of dissociation rate modification resulting from population depletion, 3) relate these atomic densities to the plasma generation process and map the spatial distribution of charged particles, 4) examine the influence of limiting forms of electron diffusive transport on flowfield structure and species distributions, and 5) confirm that the ideal plasma approximation is applicable for the plasma conditions considered.

The simplified set of the equations with suitable assumptions were solved to describe the weakly ionized flowfields of the RAM-C II flight test, simulated in the past by many other researchers. Plasma generation is restricted to the associative-ionization of nitrogen and oxygen. This simulation establishes a baseline and provides understanding of the governing equations and the limits of validity of assumptions. The magnitude of the source and sink terms were reported for the RAM-C II case to assess 1) the level of complexity of the reacton rate set required, 2) the accuracy of the reaction rates, and 3) the importance of the coupling mechanisms of the elastic collisions. Results of the simulation of the RAM-C II flight-test case show that, for the high temperature considered, the effect of depletion of vibrational population due to dissociation of nitrogen is negligible.

Simulations using two different limiting forms of the ambipolar diffusion coefficient resulted in only a minor variation in the magnitude and spatial distribution of the charged species. The simulation revealed fair agreement of the charged densities with experiment downstream of shock and extending to the body. In contrast, the comparison at the shock front suggested that inclusion of ionization through excited states or space charge effects at the shock front may be required to explain the enhanced experimental charge densities. Neutral particle diffusion plays an important role at the shock front. Elevated levels of vibrationally excited nitric oxide diffuse upstream of the front. These excited species may modify the ionization kinetics.

Future work should be directed at examining the validity of the fluid equation approach to characterizing shock structure in ionized flows by comparing the fluid results with direct simulation Monte Carlo or particle-in-cell simulations. Further research is also required to understand and refine ionization mechanisms, excited state chemistry, and collisional energy exchange.

Appendix: Reaction Rate Coefficients

Table A1 Forward reaction rate coefficients[a]

Reaction	M	C_f, (m^3/kmole · $K^{-\eta}$ s)	η	Θ_{ds}, K	Ref.
$N_2 + M \rightleftharpoons N + N + M$	N_2, O_2, NO	3.7E+18	−1.6	113,200	15
	N	1.1E+19	−1.6	113,200	15
	O	1.1E+19	−1.6	113,200	15
$O_2 + M \rightleftharpoons O + O + M$	N_2, O_2, NO	2.75E+16	−1.0	59,500	15
	N	8.25E+19	−1.0	59,500	15
	O	8.25E+19	−1.0	59,500	15
$NO + M \rightleftharpoons N + O + M$	N_2, O_2, NO	2.3E+14	0	75,500	15
	N	4.6E+14	−0.5	75,500	15
	O	4.6E+14	−0.5	75,500	15
$N_2 + O \rightleftharpoons NO + N$	——	3.18E+10	−0.1	37,700	15
$NO + O \rightleftharpoons O_2 + N$	——	2.16E+05	1.29	19,220	15
$N + O \rightleftharpoons NO^+ + e^-$	——	6.50E+08	0.00	32,000	16

[a] $k_f(T_{\text{eff}}) = C_f T_{\text{eff}}^{\eta} \exp(-\theta_{ds}/T_{\text{eff}})$.

Table A2 Constants for computing equilibrium constants used with dissociation rates of Table A1[a]

Reaction	A_{1m}	A_{2m}	A_{3m}	A_{4m}	A_{5m}	Ref.
$N_2 + M \rightleftharpoons N + N + M$	3.898	−12.611	0.683	−0.118	0.006	15
$O_2 + M \rightleftharpoons O + O + M$	1.335	−4.127	−0.616	0.093	−0.005	15
$NO + M \rightleftharpoons N + O + M$	1.549	−7.784	0.228	−0.043	0.002	15
$N_2 + O \rightleftharpoons NO + N$	2.349	−4.828	0.455	−0.075	0.004	15
$NO + O \rightleftharpoons O_2 + N$	0.215	−3.652	0.843	−0.136	0.007	15
$N + O \rightleftharpoons NO^+ + e^-$	−6.234	−5.536	0.494	−0.058	0.003	15

[a] $k_b(T_{\text{eff}}) = k_f(T_{\text{eff}})/K_{\text{eq}}(T_{\text{eff}})$ with K_{eq} units kilomole per cubic meter and exchange reactions dimensionless. The equilibrium constants for the chemical reactions computed using $K_{\text{eq}} = \exp(A_{1m} + A_{2m} Z + A_{3m} Z^2 + A_{4m} Z^3 + A_{5m} Z^4)$ where $Z = 10{,}000/T$ (T is translational temperature in Kelvin).

Acknowledgments

This research was supported under U.S. Air Force Office of Scientific Research contracts monitored by W. Hilbun and J. Schmisseur. Computer resources were provided by the U.S. Department of Defense, High Performance Computing, Major Shared Resource Center at Navy Oceanographic Office, Bay St. Louis, Mississippi.

References

[1] Lee, J., "Basic Governing Equations for the Flight Regimes of Aeroassisted Oribital Transfer Vehicles," *Thermal Design of Aeroassisted Orbital Transfer Vehicles*, Vol. 96, Progress in Astronautics and Aeronautics, AIAA, New York, 1985, pp. 3–53.

[2] Appleton, J., and Bray, K., "The Conservation Equations for a Nonequilibrium Plasma," *Journal of Fluid Mechanics*, Vol. 20, No. 4, 1964, pp. 659–672.

[3] Bedin, A., and Mishin, G., "Ballistic Studies of the Aerodynamic Drag on a Sphere in Ionized Air," *Technical Physics Letters*, Vol. 21, No. 1, 1995, pp. 5–7.

[4] Gurijanov, E., and Harsha, P., "AJAX: New Directions in Hypersonic Technology," AIAA Paper 96-4609, Nov. 1996.

[5] Ganguly, B., Bletzinger, P., and Garscadden, A., "Shock Wave Damping and Dispersion in Nonequilibrium Low Pressure Argon Plasmas," *Physics Letters A*, Vol. 230, No. 3, 1997 pp. 218–222.

[6]Hilbun, W., "Shock Waves in Nonequilibrium Gases," Ph.D. Dissertation, Dept. of Physics, U.S. Air Force Inst. of Technology, Wright–Patterson AFB, OH, 1997.

[7]Shang, J., "Recent Research in Magneto-Aerodynamics," *Progress in Aerospace Scinences*, Vol. 37, June 2001, pp. 1–20.

[8]Fomin, V., Maslov, A., Shashkin, A., Korotaeva, T., and Malmuth, N., "Flow Regimes Formed by a Counterflow Jet in a Supersonic Flow," *Journal of Applied Mechanics and Technical Physics*, Vol. 42, No. 5, 2001, pp. 757–764.

[9]Holt, E., and Haskell, R., *Foundations of Plasma Dynamics*, Macmillan, New York, 1965, pp. 151–182.

[10]Lin., S.-C., and Teare, J., "Rate of Ionization Behind Shock Waves in Air. II. Theoretical Interpretations," *Physics of Fluids*, Vol. 6, No. 3, 1963, pp. 355–375.

[11]Vincenti, W., and Kruger, C., Jr., *Introduction to Physical Gas Dynamics*, Wiley, New York, 1967, pp. 21, 197–244.

[12]Wilson, J., "Ionization Rate of Air Behind High-Speed Shock Waves," *Physics of Fluids*, Vol. 9, No. 10, 1966, pp. 1913–1921.

[13]Park, C., *Nonequilibrium Hypersonics Aerothermodynamics*, Wiley, New York, 1990, pp. 139–142.

[14]Gupta, R., Yos, J., Thompson, R., and Lee, K.-P., "A Review of Reaction Rates and Thermodynamic Properties for an 11-Species Air Model for Chemical and Thermal Nonequilibrium Calculations to 30,000 K," NASA RP, TR 1232, Aug. 1987.

[15]Park, C., "On Convergence of Computation of Chemically Reacting Flows," AIAA Paper 85-0247, Jan. 1985.

[16]Wray, K., "Chemical Kinetics of High Temperature Air," *Hypersonic Flow Research*, edited by F. R. Riddell, Vol. 7, ARS Progress in Astronautics and Rocketry, Academic Press, New York, 1962, pp. 181–204.

[17]Park, C., "Assessment of Two-Temperature Kinetic Model for Ionizing Air," *Journal of Thermophysics and Heat Transfer*, Vol. 3, No. 3, 1989, pp. 233–244.

[18]Park, C., "Calculation of Real-Gas Effects on Blunt-Body Trim Angels," *AIAA Journal*, Vol. 30, No. 4, 1992, pp. 999–1006.

[19]Bose, D., and Candler, G., "Simulation of Hypersonic Flows Using a Detailed Nitric Oxide Formation Model," *Physics of Fluids*, Vol. 9, No. 4, 1997, pp. 1171–1181.

[20]Blottner, F., Johnson, M., and Ellis, M., "Chemically Reacting Viscous Flow-Program for Multicomponent Gas Mixtures," Sandia Labs., TR SC-RR-70-754, Albuquerque, NM, Dec. 1971.

[21]Wilke, C., "A Viscosity Equation for Gas Mixtures," *Journal of Chemical Physics*, Vol. 18, No. 4, 1950, p. 517.

[22]Rose, P., and Stankevis, J., "Stagnation-Point Heat Transfer Measurements in Partially Ionized Air," *AIAA Journal*, Vol. 1, No. 12, 1963, pp. 2752–2763.

[23]Cussler, E., *Diffusion*, Cambridge Univ. Press, New York, 1984.

[24]Kolesnikov, A., and Tirskii, G., "The Stefan–Maxwell Equations for Diffusion Fluxes of Plasma in a Magnetic Field," *Fluid Dynamics*, Vol. 9, No. 4, 1984, pp. 643–649.

[25]Kolesnikov, A., "Mechanism of the Ion Baro-Thermal-Diffusion Pumping in Weakly Ionized Shock Layer," AIAA Paper 2001-2871, June 2001.

[26]Bird, R., Stewart, W., and Lightfoot, E., *Transport Phenomena*, Wiley, New York, 1960.

[27]Candler, G., and MacCormack, R., "Computation of Weakly Ionized Hypersonic Flows in Thermochemical Nonequilibrium," *Journal of Thermophysics and Heat Transfer*, Vol. 5, No. 3, 1991, pp. 266–273.

[28]Landau, L., and Teller, E., "Zur Theorie der Schalldispersion," *Physikalische Zeitschrift der Sowjetunion*, Vol. 10, No. 1, 1936, pp. 34–43.

[29]Josyula, E., and Bailey, W., "Vibration–Dissociation Coupling Using Master Equations in Nonequlibrium Hypersonic Blunt-Body Flow," *Journal of Thermophysics and Heat Tansfer*, Vol. 15, No. 2, 2001, pp. 157–167.

[30]Josyula, E., "Computational Study of Vibrationally Relaxing Gas Past Blunt Body in Hypersonics Flows," *Journal of Thermophysics and Heat Transfer*, Vol. 14, No. 1, 2000, pp. 18–26.

[31]Millikan, R., and White, D., "Systematics of Vibrational Relaxation," *Journal of Chemical Physics*, Vol. 39, No. 12, 1963, pp. 3209–3213.

[32]Josyula, E., and Bailey, W., "Vibrational Relaxation and Population Depletion of Nitrogen in Hypersonic Flows," AIAA Paper 2002-0200, Jan. 2002.

[33]Park, C., "Assessment of Two-Temperature Kinetic Model for Dissociating and Weakly-Ionizing Nitrogen," AIAA Paper 86-1347, 1986.

[34]Park, C., "Assessment of Two-Temperature Kinetic Model for Ionizing Air," AIAA Paper 87-1574, 1987.

[35]Lee, J., "Electron-Impact Vibrational Excitation Rates in the Flowfield of Aeroassisted Orbital Transfer Vehicles," *Thermophysical Aspects of Re-Entry Flows*, Vol. 103, Progress in Astronautics and Aeronautics, AIAA, New York, 1986, pp. 197–224.

[36]Walters, R., Cinnella, P., and Slack, D., "Characteristic-Based Algorithms for Flows in Thermochemical Non-Equilibrium," *AIAA Journal*, Vol. 30, No. 5, 1992, pp. 1304–1313.

[37]Josyula, E., and Shang, J., "Computation of Noneqilibrium Hypersonic Flowfields past Hemisphere Cylinder," *Journal of Thermophysics and Heat Transfer*, Vol. 7, No. 4, 1993, pp. 668–679.

[38]MacCormack, R., "Current Status of Numerical Solutions of the Navier–Stokes Equations," AIAA Paper 85-0032, 1985.

[39]Cinnella, P., and Grossman, B., "Upwind Techniques for Flows with Multiple Translational Temperatures," AIAA Paper 90-1660, June 1990.

[40]Grossman, B., Cinnella, P., and Eppard, W., "New Developments Pertaining to Algorithms for Non-Equilibrium Hypersonic Flows," *Computational Fluid Dynamics Journal*, Vol. 1, No. 2, 1992, pp. 175–186.

[41]Taylor, J., Olynick, D., and Hassan, H., "Upwind Techniques for Ionized Flows," AIAA Paper 94-1957, June 1994.

[42]Roache, P., *Verification and Validation in Computational Science and Engineering*, Hermosa, Albuquerque, NM, 1998, pp. 107–142.

[43]Kaegi, E., and McMenamin, D., Jr., "Measured and Predicted Air Ionization in Blunt Body Shock Layers," AIAA Paper 69-81, Jan. 1969.

[44]Akey, N., and Cross, M., "Radio Blackout Alleviation and Plasma Diagnostic Results from a 25,000 Foot per Second Blunt Body Reentry," NASA TR D-5615, Feb. 1970.

[45]Grantham, W., "Flight Results of 25,000 Foot per Second Reentry Experiment Using Microwave Reflectometers to Measure Plasma Electron Density and Standoff Distance," NASA TR D-6062, Dec. 1970.

[46]Jones, W., Jr., and Cross, M., "Electrostatic Probe Measurements of Plasma Parameters for Two Reentry Flight Experiments at 25,000 Feet per Second," NASA TR D-6617, Feb. 1972.

[47]Grasso, F., and Capano, G., "Modeling of Ionizing Hypersonic Flows in Nonequilibrium," *Journal of Spacecraft and Rockets*, Vol. 32, No. 2, 1995, pp. 217–224.

[48]Candler, G., "The Computation of Weakly Ionized Hypersonic Flows in Thermo Chemical Nonequilibrium," Ph.D. Dissertation, Dept. of Aeronautics and Astronautics, Stanford Univ., Stanford, CA, 1988.

[49]Josyula, E., and Bailey, W. F., "Vibration–Dissociation Coupling Model for Hypersonic Blunt-Body Flow," *AIAA Journal*, Vol. 41, No. 8, 2003, pp. 1611–1613.

B. Hassan
Associate Editor